Journal of Advanced Ceramics
2024, **13**(3): 388–401
https://doi.org/10.26599/JAC.2024.9220863

Research Article

Durable dual-state duplex Si–HfO_2 with excellent oxidation and cracking resistance

Lin Chen[1,†], Jing-Chuan Luo[1,†], Wen-Qi Yang[2], Chang-Jiu Li[1], Guan-Jun Yang[1,✉]

[1] *State Key Laboratory for Mechanical Behavior of Materials, School of Materials Science and Engineering, Xi'an Jiaotong University, Xi'an 710049, China*
[2] *Xi'an Aerospace Engine Company Limited in CASC, Xi'an 710065, China*

Received: December 7, 2023; Revised: January 23, 2024; Accepted: February 4, 2024

Abstract: The lifetime of Si bond coatings in environmental barrier coatings is constrained by phase-transition-induced cracking of the SiO_2 scale. In this study, Si–HfO_2 dual-state duplex composite materials are proposed to address this issue by partially forming $HfSiO_4$ and minimizing the SiO_2 content. The as-prepared composite exhibited a structure comprising discrete HfO_2 "bricks" embedded in a continuous Si "mortar", while the oxidized state transformed into discrete $HfSiO_4$ "bricks" within continuous thin SiO_2 "mortars". The results indicate that continuous thin SiO_2 contributes to reducing the oxidation rate to a level comparable to that of pure Si, and discrete $HfSiO_4$ particles aid in relieving phase transition-induced stress and inhibiting crack propagation, thereby enhancing oxidation and cracking resistance simultaneously. Consequently, the composite with 20 mol% HfO_2 and a mean particle size of ~500 nm at 1370 ℃ exhibited a service lifetime 10 times greater than that of pure Si. This research provides valuable insights for designing Si-based bond coatings with improved service lifetime.

Keywords: environmental barrier coatings (EBCs); bond coatings; oxidation; phase transition; cracking

1 Introduction

Ceramic matrix composites (CMCs), especially SiC_f/SiC_m, are being used in new generations of propulsion materials in high-pressure turbines due to their excellent high-temperature mechanical properties [1,2]. However, they suffer from rapid recession by water vapor and oxidizers in gas turbine environments [3,4]. Environmental barrier coatings (EBCs) are used as key protection agents for inhibiting the rapid recession of SiC_f/SiC_m composites [5–7]. EBCs typically consist of a Si bond coating and a rare-earth silicate top coating [8]. During service at ≥ 1300 ℃, a SiO_2 thermally grown oxide (TGO) layer is produced between the Si bond coating and the top coating, which is primarily composed of β-cristobalite [9,10]. However, the transformation from β-cristobalite to α-cristobalite occurs at ~220 ℃ and is accompanied by a 4.5% volume contraction [8,11]. As a result, large elastic strain energy is generated, causing severe TGO microcracking and premature spalling of the EBCs [12,13]. Therefore, suppressing the SiO_2 phase transition is extremely important for realizing long-lifetime operation of EBCs.

To eliminate this unexpected phase transition, Si-stabilizer (Al_2O_3 or mullite) duplex coatings and Si–HfO_2 composite coatings have been proposed [14]. In Si-stabilizer duplex coatings, the diffusion of Al from the stabilizer to the SiO_2 scale causes high-temperature β-SiO_2 to retain metastability at room temperature, thus preventing phase-transition-induced cracking. However, the SiO_2 growth rates in Si-stabilizer duplex coatings are twice as high as those in pure Si coatings at 1350 ℃ due to the entry of Al^{3+} into the crystalline SiO_2 lattice, leading to the formation of additional oxygen vacancies. In Si–HfO_2 composite coatings, suppression of the phase transition relies on the reaction between SiO_2 and HfO_2 to form $HfSiO_4$ [13,15,16]. Nevertheless, the continuous HfO_2 phase in the composite serves as an oxygen conduit, and the discontinuous Si phase has a high surface area. Once Si is oxidized, the composite coating will not provide any effective protection to the SiC substrate, resulting in premature cracking along the coating/substrate interface [17,18]. These findings underscore the limitations of Si–HfO_2 composite coatings in achieving long lifetime operation of EBCs.

The limitations of Si–HfO_2 composite coatings stem from the inappropriate distribution of the HfO_2 phase [13,15,16]. On the one hand, oxidation of the SiC substrate can be avoided if the HfO_2 phase exhibits a discrete distribution. On the other hand, the HfO_2 particle size inside the composite coating should be redesigned to achieve a synergistic effect between the oxidation (formation of SiO_2) and reaction (formation of $HfSiO_4$) kinetics, thereby minimizing the amount of SiO_2. Therefore, Si–HfO_2 composite coatings can simultaneously inhibit phase transitions and reduce oxidation rates. To increase the service lifetime, careful consideration of the HfO_2 content and distribution is paramount. However, Si–HfO_2 composite coatings reportedly exhibit high HfO_2 content (> 36 mol%) and a continuous distribution [13,15,16].

This study introduces a novel Si–HfO_2 dual-state duplex composite structure with discrete HfO_2 "bricks" and continuous Si "mortars" in the as-prepared state. After oxidation, it transforms into a structure with discrete $HfSiO_4$ "bricks" and

† Lin Chen and Jing-Chuan Luo contributed equally to this work.
✉ Corresponding author.
E-mail: ygj@mail.xjtu.edu.cn

continuous thin SiO_2 "mortars". Continuous thin SiO_2 reduces the oxidation rate, and discrete $HfSiO_4$ particles alleviate phase-transition-induced stress, thereby enhancing the oxidation and cracking resistance simultaneously. Compared to that of pure Si, the composite shows a 10-fold longer service lifetime at 1370 ℃, with a comparable oxidation rate. This research offers insights into designing Si-based composite bond coatings with enhanced service lifetime for EBCs.

2 Design of the Si–HfO_2 dual-state duplex composite structure

The phase transition of SiO_2 causes a 4.5% volume contraction, which produces a large elastic strain energy inside the SiO_2 scale [8,11]. However, SiO_2 has a low fracture toughness [10]. Consequently, severe cracking or spallation occurred (Fig. 1(a)). For channel cracking, the critical TGO thickness (h_c) dictates

$$h_c = \frac{\gamma}{g_0 \varepsilon_0^2 \bar{E}} \tag{1}$$

where ε_0, g_0, and γ are the phase-transition-induced strain (~1%) [10], dimensionless parameter, and fracture energy, respectively. $\bar{E} = E_0/(1-\nu_0^2)$ is the plane strain modulus, where E_0 and ν_0 are the modulus and Poisson's ratio of SiO_2 TGO, respectively. Below the critical thickness, channel cracking is suppressed. For the pure Si coating, the h_c value is estimated to be 1.3 μm, which is consistent with the reported experimental value of ~1.5 μm [8,13].

During the oxidation of the Si–HfO_2 composite, both SiO_2 and $HfSiO_4$ formed, and the SiO_2 scale was divided by $HfSiO_4$ particles (Fig. 1(b)). $HfSiO_4$ has a greater fracture toughness than SiO_2

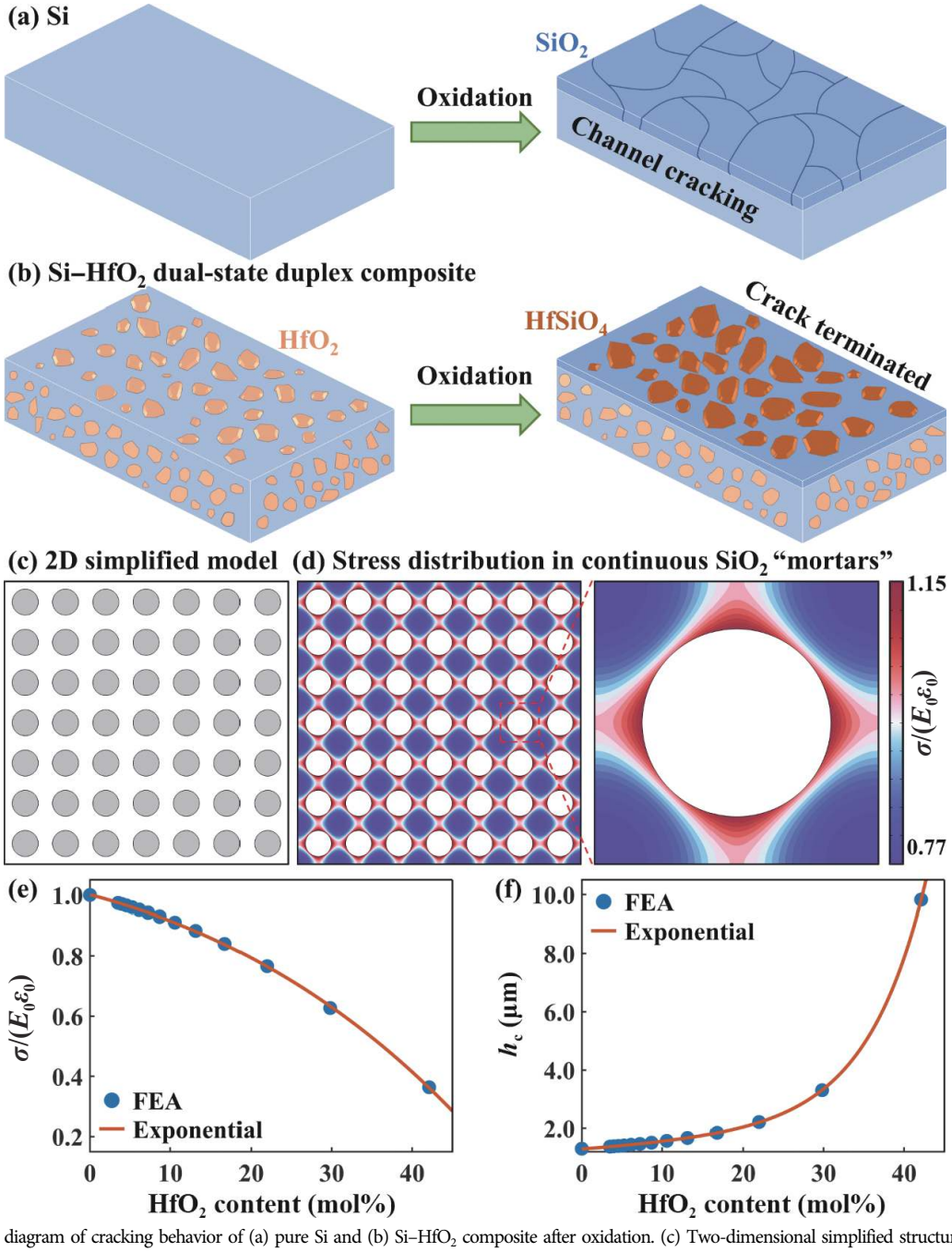

Fig. 1 Schematic diagram of cracking behavior of (a) pure Si and (b) Si–HfO_2 composite after oxidation. (c) Two-dimensional simplified structure of the Si–HfO_2 composite and (d) stress distribution after the SiO_2 phase transition, (e) dependence of stress and (f) critical thickness on the HfO_2 content in the Si–HfO_2 composites.

[19,20]. As a result, when a crack encounters an $HfSiO_4$ particle, propagation occurs along the $HfSiO_4$–SiO_2 interface. Compared with those in the pure Si sample, the cracks in the Si–HfO_2 composite exhibited more zigzag shapes, indicating greater cracking resistance. Moreover, when Si oxidizes to SiO_2 and then transforms to $HfSiO_4$, the volume increase is calculated to be 14.8% [13,21]. Thus, $HfSiO_4$ grows under compressive stress. The residual compressive stress helps to alleviate the tensile stresses caused by the SiO_2 phase transition. As expected, $HfSiO_4$ particles result in stress redistribution in SiO_2 and the formation of a stress relief zone. To demonstrate the stress release, a 2D simplified model consisting of SiO_2 and $HfSiO_4$ was constructed (Fig. 1(c)), and finite element analysis (FEA) was conducted. The FEA results confirmed the existence of a stress relief zone (Fig. 1(d)). The stress relief relies on the HfO_2 content and follows an exponential relationship (Fig. 1(e)). Moreover, stress relief contributes to increasing the critical TGO thickness (h_c, Fig. 1(f)). Compared to that of pure Si, the stress in the Si–HfO_2 composite with 20 mol% HfO_2 was reduced by 25% (Fig. 1(e)). This resulted in a 78% increase in the critical TGO thickness (Fig. 1(f)). These results indicate that the addition of HfO_2 to the Si–HfO_2 composite contributes to both reducing the cracking stress and increasing the cracking resistance.

To completely eliminate the SiO_2 phase transition, a Si–HfO_2 composite with 50 mol% HfO_2 is optimal. However, both HfO_2 and $HfSiO_4$ are oxygen conduits [17]. A high HfO_2 content inevitably results in the continuous distribution of HfO_2 and $HfSiO_4$, thus reducing its oxidation resistance. In addition, the coefficient of thermal expansion (CTE) of HfO_2 is 6.46×10^{-6}–7.72×10^{-6} K^{-1} [15–17,22], which is higher than that of SiC_f/SiC CMCs [10]. Therefore, a higher HfO_2 content produces a greater thermal mismatch stress during thermal cycling, causing premature cracking and delamination [15,18]. Therefore, it is important to control the HfO_2 content to balance the need for antioxidation and anti-cracking.

In response to these challenges, this study proposes a new Si–HfO_2 dual-state duplex composite structure. The as-prepared composite consists of discrete HfO_2 "bricks" and continuous Si "mortars", transforming into a structure with discrete $HfSiO_4$ "bricks" and continuous thin SiO_2 "mortars" after oxidation. This design aims to simultaneously reduce the oxidation rate and relieve phase-transition-induced stress.

3 Experimental

3.1 Composite preparation and isothermal oxidation

It is crucial to highlight that both HfO_2 and $HfSiO_4$ function as oxygen conduits [17,21]. Consequently, a discrete distribution of HfO_2 particles in the Si–HfO_2 composite is imperative. To obtain a discrete distribution of HfO_2 particles, the sizes of the Si powders must be smaller than those of the HfO_2 powders. However, this consideration was often overlooked in prior studies [15,16,23], leading to rapid oxidation of Si and SiC substrates. According to fracture mechanics, smaller particle sizes with the same HfO_2 content indicate greater cracking resistance [24]. However, smaller particles exhibit lower thermal stability, leading to Ostwald ripening [13,19]. HfO_2 particles of ~280 nm in size have demonstrated stability for 1000 h at 1250 ℃ [13]. To ensure thermal stability at 1370 ℃, HfO_2 particles ranging in size from 300 to 800 nm were selected.

In an effort to suppress the SiO_2 phase transition, a high concentration of HfO_2 (> 36 mol%) was incorporated into Si–HfO_2 composite coatings [13,16,23,25]. However, a high HfO_2 content results in a continuous distribution of HfO_2 particles. Although lower HfO_2 contents (< 25 mol%) have been explored, reported Si–HfO_2 composite coatings still exhibit a continuous distribution of HfO_2 particles due to the larger Si particle size compared to that of HfO_2 [15,17]. In this study, Si–HfO_2 samples were prepared with HfO_2 contents of 10 mol%, 20 mol%, and 30 mol%, denoted as Si10Hf, Si20Hf, and Si30Hf, respectively. The Si powders (99.99%, Shanghai STNANO Science & Technology Co., Ltd.) ranged from 100 to 200 nm in size. Dual-scale HfO_2 raw powders were utilized for Si–HfO_2 composite preparation, in which finer HfO_2 powders (500–1500 nm, 99.99%, Quannan Jingxin Environmental Protection Materials Co., Ltd.) were incorporated to eliminate SiO_2 and coarser particles (2–10 μm) to enhance the creep strength at 1370 ℃ [17,18]. According to stoichiometric ratios, Si and HfO_2 powders were mixed through ball milling in a Si_3N_4 jar with ZrO_2 balls for 12 h at a rotation speed of 5 $r{\cdot}s^{-1}$. The diameter of the milling jar was 50 mm. The ball-to-powder mass ratio was 8 : 1. Hydraulic pressing (at 300 MPa pressure) was used to form green bodies with a diameter of 10 mm and a thickness of 1 mm. The subsequent dense Si–HfO_2 composites were prepared through two-step sintering in an argon atmosphere, initially at 1100 ℃ for 20 h, followed by 1370 ℃ for 8 h, with a heating and cooling rate of 4 ℃·min^{-1}.

For the isothermal oxidation test, the detailed procedures can be found in Refs. [10,14]. The melting point of Si is 1414 ℃, which can be substantially lower in the presence of impurities. This limits the use temperature of Si coatings to typically less than 1316 ℃ [17]. In addition, the oxidation of Si coatings is sensitive to temperature [14]. Therefore, to accelerate the evaluation of the oxidation kinetics and failure behaviors of the composites, the oxidation temperature in this study was set to 1370 ℃. Oxidation at 1300 ℃ was also conducted for comparison. Isothermal durations included 5, 10, 50, 100, 150, and 200 h, with a heating and cooling rate of 4 ℃·min^{-1} during oxidation.

3.2 Microstructural characterization

The surface and cross-sectional microstructures of the composites were examined using scanning electron microscopy (SEM, VEGA II-XMU, TESCAN). The elemental distributions were analyzed via energy dispersive spectroscopy (EDS, AZTEC, Oxford Instruments) integrated into the SEM. The acceleration voltage and working distance used for EDS testing were 15 kV and 15 mm, respectively. The X-ray diffraction (XRD, D8advance 3.0, Bruker) was utilized to identify the phase composition within a 2θ range of 10°–90°. The samples were scanned with a step size of 0.1° and a velocity of 2 (°)·min^{-1}. Semi-quantitative analysis of the relative phase composition was conducted by comparing peak intensities [12,26,27]. Additionally, TGO thickness was measured via Demo VegaTC software, which was integrated into the SEM.

The atomic structures were investigated through scanning transmission electron microscope (FSTEM, JEM-F200, operating at 200 kV). TEM samples were prepared using a focused ion beam (FIB, FEI Quanta 200 FEG). Amorphous layers generated during FIB preparation were removed using a Nano Mill (M1040 Nano Mill, Fischione) with argon ions (Ar^+) as the cleaning agent at an ion energy of 700 eV and a milling angle of 30°. The faces of the samples were milled for 30 min. The fracture toughness of the sintered composites was measured through Vickers hardness indentation at a load of 1 kgf with a dwell time of 10 s. A nanoindentation test was conducted with an Agilent Nano Indenter G200 instrument at a load of 150 mN and a dwell time

of 10 s to obtain the modulus.

The surface/interface energies and density of states of $HfSiO_4$–SiO_2 and HfO_2–SiO_2 were investigated through first-principles calculations. Structures and surfaces were constructed using Materials Studio software, and calculations were performed in the Vienna *ab initio* simulation package (VASP). Electronic exchange-correlation interactions were handled with projector augmented wave (PAW) and generalized-gradient approximation (GGA) using the Perdew, Burke, and Ernzerhof (PBE) pseudopotential. The cutoff energy of the plane wavefunction was set to 350 eV, and *K*-points were set to 4×4×6. Geometry optimizations were performed using conjugate gradient minimization until all the forces acting on the ions were less than 10^{-8} eV·Å^{-1} per atom. *Ab initio* molecular dynamics simulations of the optimized structures were performed using DFT semi-pseudo-potential processing kernels, NVT ensembles, atmospheric pressure, a temperature of 1400 ℃, and a time step of 1 fs for a total simulation time of 10 ps.

4 Results

4.1 Phase composition and microstructure of the as-prepared Si–HfO_2 composites

Due to the two-step sintering process with an argon atmosphere, dense Si–HfO_2 composites were prepared (Figs. 2(a) and 2(b)). The Feret diameter distribution of the HfO_2 particles was measured using ImageJ software at a magnification of 5000 times. The statistical area was > 26,000 μm^2. The HfO_2 particle size ranges from approximately 300 to 800 nm, with an average value of ~500 nm in the composite. During composite preparation, only Si (cubic) and HfO_2 (monoclinic, m-HfO_2) phases were detected (Fig. 2(c)). This indicates that HfO_2 and Si can form a stable composite structure at 1370 ℃. The main peaks of the Si and m-HfO_2 phases are at (111), with corresponding 2θ values of 28.4° and 31.7°, respectively. The HfO_2 phase contents in the as-prepared Si10Hf, Si20Hf, and Si30Hf composites were estimated to be 13, 20, and 29 mol%, respectively, which were consistent with the set values. Compared with that of pure Si, the fracture toughness of the Si10Hf, Si20Hf, and Si30Hf composites increased by 20%, 44%, and 131%, respectively (Fig. 2(d)). This is consistent with the reported values ranging between 1.38 and 1.52 MPa·m$^{1/2}$ for the Si-rich phase and between 2.26 and 2.38 MPa·m$^{1/2}$ for the HfO_2-rich phase [20]. Figure 2(e) shows the load-displacement curves of the as-prepared composites. According to the hysteresis, the moduli for Si, Si10Hf, Si20Hf, and Si30Hf are estimated to be 183, 144, 139, and 154 GPa, respectively. This is consistent with the reported values of 205 and 157 GPa for pure Si and Si–HfO_2 composites, respectively (with 36 mol% HfO_2) [28]. Compared with that of pure Si, the modulus of Si20Hf decreases by 25%, indicating a higher strain tolerance [29]. These results underscore the stability achieved at 1370 ℃ for Si–HfO_2 composites with a mean particle size of ~500 nm and the beneficial influence of HfO_2 on the fracture toughness of Si–HfO_2 composites.

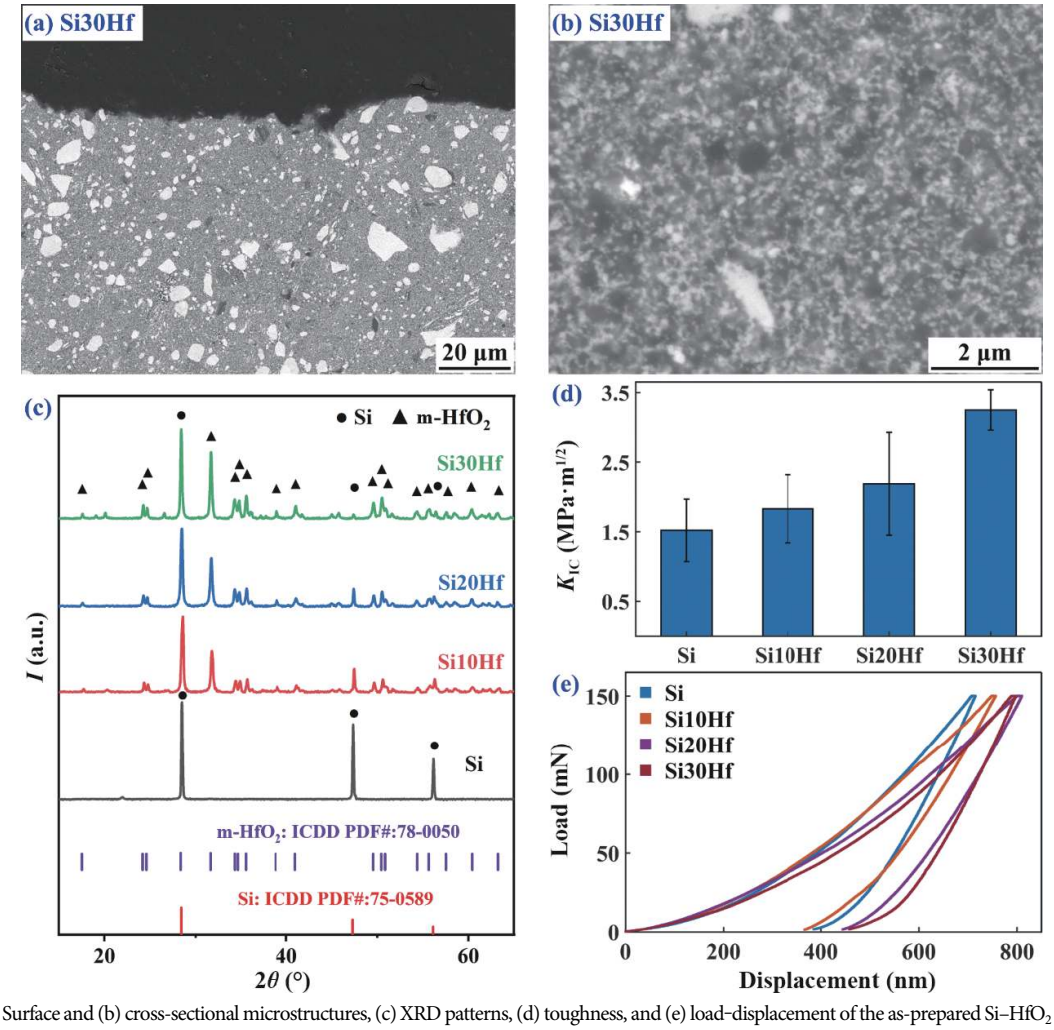

Fig. 2 (a) Surface and (b) cross-sectional microstructures, (c) XRD patterns, (d) toughness, and (e) load-displacement of the as-prepared Si–HfO_2 composites.

4.2 Structural evolutions during isothermal oxidation

Figure 3 shows the XRD patterns of the thermally grown oxides at room temperature. The tetragonal $HfSiO_4$ phase was detected after 5 h of oxidation at 1370 ℃ (Figs. 3(a)–3(c)), confirming the rapid reaction between SiO_2 and HfO_2 [30]. Moreover, the α-SiO_2 phase was detected, indicating the occurrence of the β → α phase transition [10,13]. It has been reported that Al^{3+} can enter the lattice of crystalline SiO_2, thus suppressing the β → α phase transition [14,27,31]. However, only the α-SiO_2 phase was detected in this study, indicating that HfO_2 addition cannot suppress the β → α phase transition by a lattice solid. This may be because the ionic radius of Hf^{4+} (0.83 Å) is much larger than the ionic radius of Si^{4+} (0.54 Å) [32]. As a result, HfO_2 is insoluble in crystalline SiO_2. The main peaks of the tetragonal α-SiO_2 and $HfSiO_4$ phases are at (200), with corresponding 2θ values of 36.0° and 27.1°, respectively. In addition, compared with those of the α-SiO_2 phase, higher peak intensities of the $HfSiO_4$ phase were observed (Figs. 3(a)–3(c)). This indicates the synergistic effects of oxidation (formation of SiO_2) and reaction (formation of $HfSiO_4$) kinetics. This is consistent with the report that the net thickness of SiO_2 on a Si–HfO_2 duplex decreased by at least a factor of two compared to that on pure Si [30]. In contrast to that of the as-prepared composites (Fig. 2((c)), the main peak of the m-HfO_2 phase is at (300), with a corresponding 2θ value of 54.4°. In addition, compared with that of the HfO_2 phase, the $HfSiO_4$ phase content significantly increased (Fig. 3(d)). This suggests the

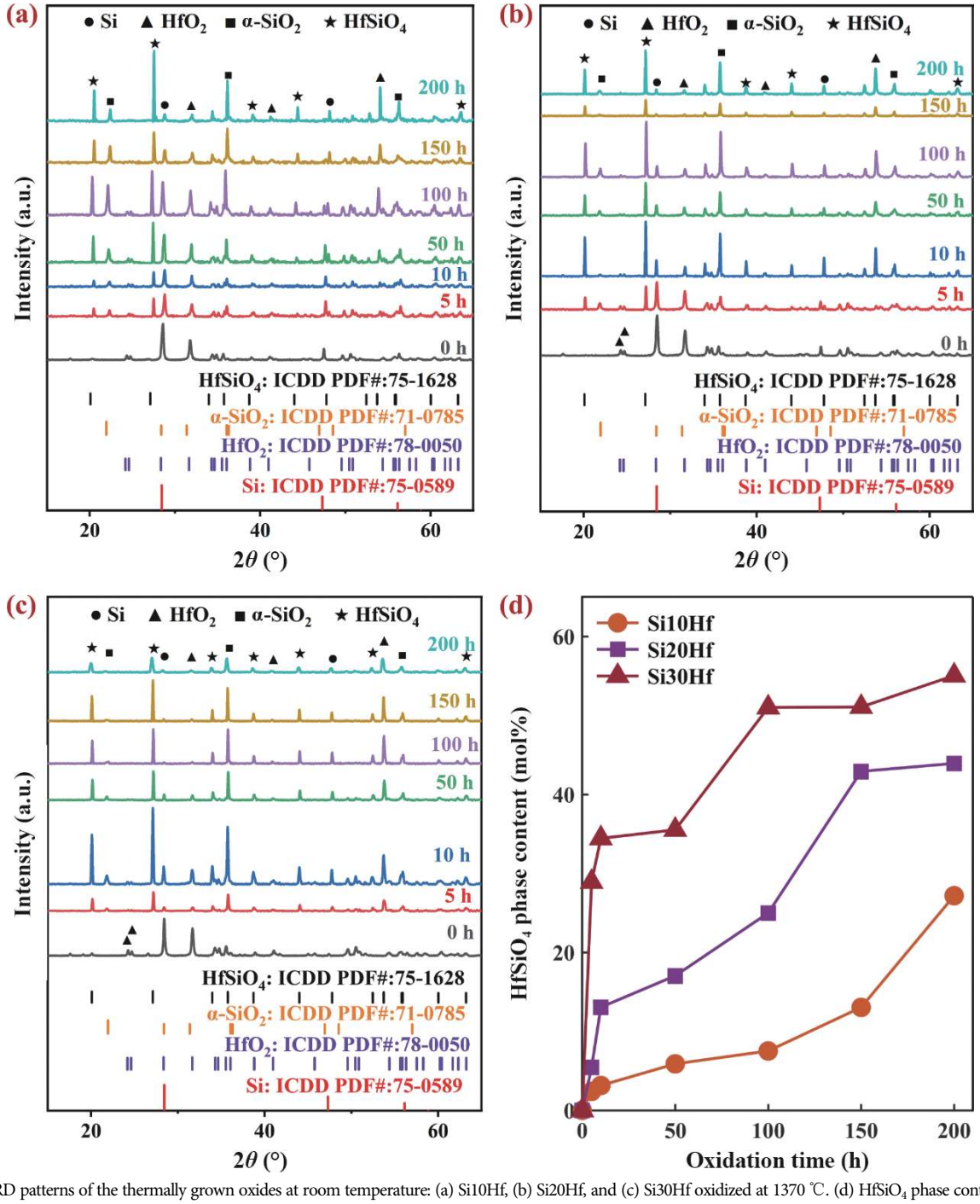

Fig. 3 XRD patterns of the thermally grown oxides at room temperature: (a) Si10Hf, (b) Si20Hf, and (c) Si30Hf oxidized at 1370 ℃. (d) $HfSiO_4$ phase content versus oxidation time.

enrichment of $HfSiO_4$ particles on the surface and the occurrence of phase separation between $HfSiO_4$ and SiO_2. These results indicate that the SiO_2 phase transition was partially eliminated by the formation of $HfSiO_4$. Therefore, determining the distribution of HfO_2 particles in composites is crucial for minimizing the SiO_2 content.

Figure 4 shows the surface morphologies of the Si–HfO_2 composites after oxidation at 1370 ℃. With increasing oxidation time, the $HfSiO_4$ particles agglomerate (Figs. 4(b), 4(d), and 4(f)), which is consistent with the XRD observations (Fig. 3(d)). Notably, networked cracks appeared on the surface of the Si10Hf composite after 100 h of oxidation (Fig. 4(b)). However, few discrete cracks were observed on the surface of the Si20Hf and Si30Hf composites after 100 h of oxidation (Figs. 4(d) and 4(f)). In comparison, networked cracks were observed on the surface of the pure Si coatings after 10 h of oxidation at 1300 ℃ [10,14]. In this study, the lifetime was defined on the basis of the integrity of TGO [14], namely, its ability to protect the underlying composite from oxidation. These results indicate that, compared with the service lifetime of pure Si, the lifetime of the Si20Hf and Si30Hf composites at 1370 ℃ increase by more than 10 times. Furthermore, compared with those of the Si20Hf composite, the HfO_2 and $HfSiO_4$ phases exhibit a continuous distribution in the Si30Hf composite (Fig. 4(f)). The continuous HfO_2 and $HfSiO_4$ phases act as oxygen conduits, probably resulting in accelerated oxidation [17]. These results indicate that the Si–HfO_2 composites with 20 mol% HfO_2 have optimal resistance to cracking and oxidation.

Figure 5 shows the cross-sectional microstructures of the Si–HfO_2 composites after oxidation. The HfO_2 particles maintained a mean size of ~500 nm inside the composites, comparable to that of the as-prepared composites (Fig. 2(a)), signifying high thermal stability at 1370 ℃. This is consistent with the finding that HfO_2 particles ~350 nm in size remained stable for 1000 h at 1250 ℃ [13]. However, compared with that of the HfO_2 particles, the size of the $HfSiO_4$ particles significantly increased. Additionally, in agreement with the XRD results (Fig. 3(d)), $HfSiO_4$ particles were enriched on the surface of the SiO_2 scale, confirming the occurrence of phase separation between $HfSiO_4$ and SiO_2. A similar phenomenon was noted for Si–HfO_2

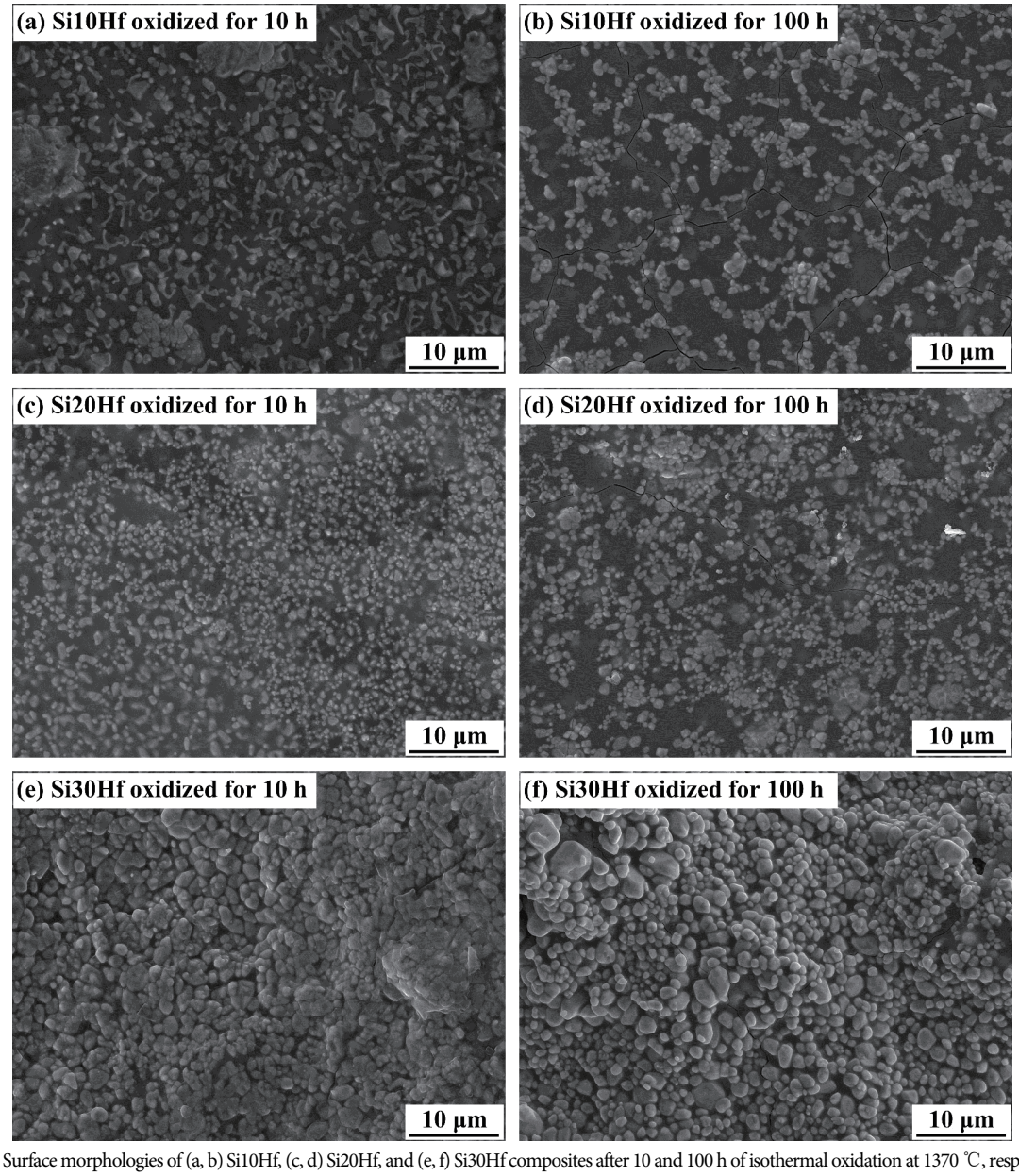

Fig. 4 Surface morphologies of (a, b) Si10Hf, (c, d) Si20Hf, and (e, f) Si30Hf composites after 10 and 100 h of isothermal oxidation at 1370 ℃, respectively.

coatings during oxidation at 1250 ℃ [13]. The observed phase separation is not conducive to inhibiting phase-transition-induced cracking. Notably, no delamination occurred at the interface between the SiO_2 scale and the Si–HfO_2 composite after 100 h of oxidation at 1370 ℃. In contrast, interfacial delamination was evident in pure Si after 20 h of oxidation at 1300 ℃, where it reached a spallation area ratio of 50% after 48 h of oxidation at 1350 ℃ [10,14]. These results indicate that HfO_2 particles with a mean value of ~500 nm have high thermal stability at 1370 ℃ and that HfO_2 addition greatly extends the cracking resistance of pure Si.

4.3 Si oxidation kinetics

The growth of SiO_2 TGOs on pure Si coatings follows a parabolic law [10,14]. Parabolic kinetics imply that the growth rate relies on oxygen transport in SiO_2 TGOs through grain boundary diffusion [14,33]. Despite HfO_2 serving as an oxygen conduit, the oxidation of Si–HfO_2 composites also follows parabolic kinetics (Fig. 6). The fitted growth rates are presented in Table 1. For pure Si, the oxidation rates are 0.46 and 0.61 μm·h$^{-1/2}$ at 1300 and 1370 ℃, respectively, which are consistent with the reported values of 0.5 μm·h$^{-1/2}$ at 1300 ℃ [10,14]. However, smaller and larger values of 0.16 and 1.2 μm·h$^{-1/2}$ are reported for pure Si coatings at 1250 and 1350 ℃, respectively [13,14], suggesting that temperature significantly influences the oxidation rate of the pure Si coating. Due to the discrete distribution of HfO_2 particles and the continuous thin SiO_2 "mortars" (Figs. 4(b) and 4(d)), the Si10Hf and Si20Hf composites exhibit oxidation rates comparable to those of pure Si at both 1300 and 1370 ℃ (Table 1). This is attributed to the HfO_2 powder being larger than the Si powder during composite preparation. In contrast, a composite structure with ~100 nm HfO_2 and ~10 μm Si exhibited a continuous distribution of HfO_2, resulting in SiC substrate oxidation [15]. These results indicate that, in contrast to reported Si–HfO_2 powders with larger Si particle sizes than HfO_2 [15,16,18,25], the smaller Si particle size contributes to the discrete distribution of HfO_2.

Due to the continuous distribution of HfO_2 particles and discrete SiO_2 "mortars" (Figs. 4(f) and 5(f)), the oxidation rates of the Si30Hf composites are 1.6 and 1.8 times greater than those of pure Si at 1300 and 1370 ℃, respectively (Table 1). This finding aligns with a previous report indicating complete oxidation of free

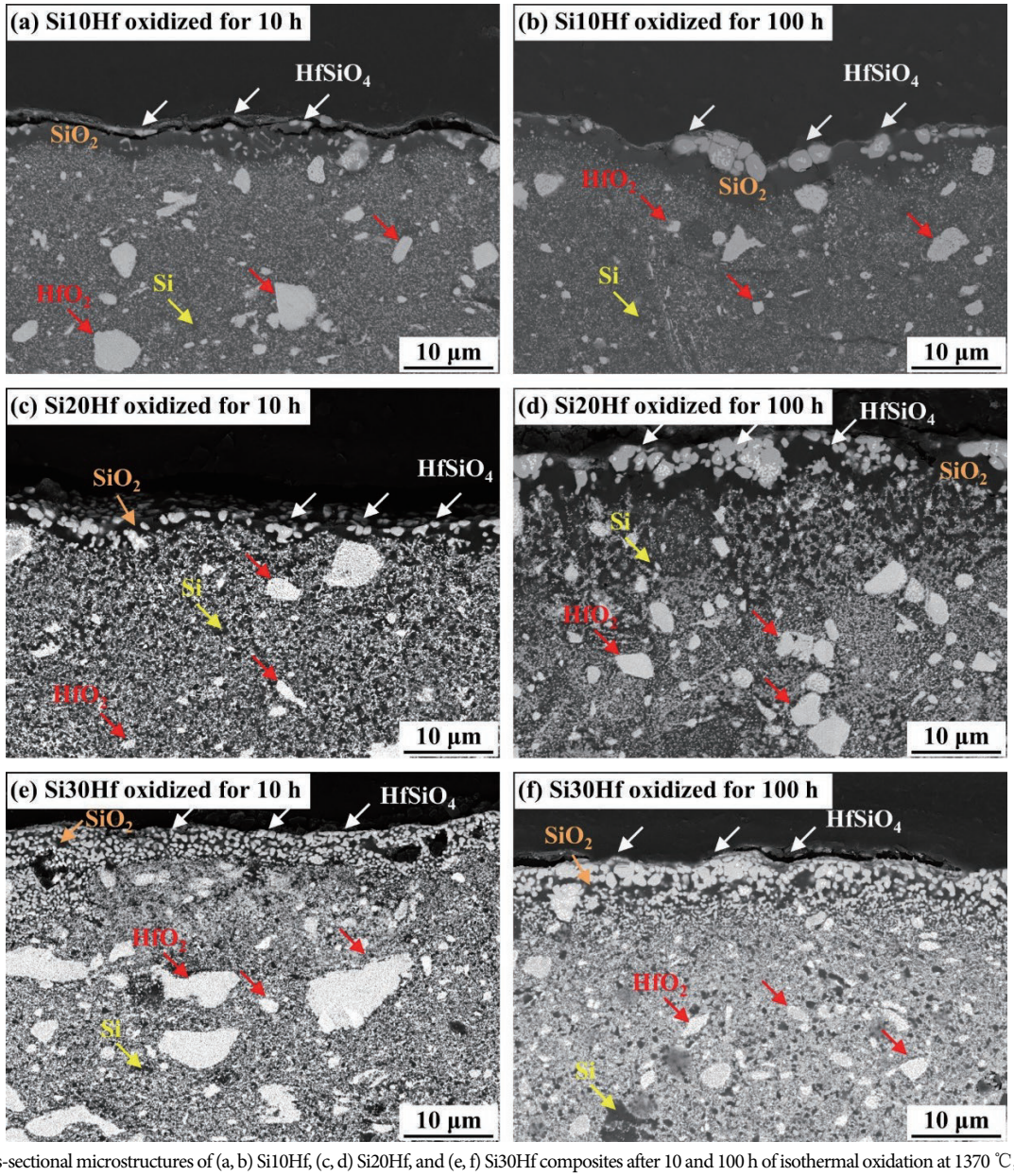

Fig. 5 Cross-sectional microstructures of (a, b) Si10Hf, (c, d) Si20Hf, and (e, f) Si30Hf composites after 10 and 100 h of isothermal oxidation at 1370 ℃, respectively.

Si inside a 50 μm thick Si–HfO_2 coating (25/75 mol% HfO_2/Si) within 10 h at 1370 ℃ [17]. The oxidation rate is 16.3 times that of the Si30Hf composite. Additionally, the fitted oxidation rates are approximately 2.2 and 2.1 μm·$h^{-1/2}$ for the Si–Al_2O_3 and Si–mullite duplex coatings, respectively, at 1350 ℃ [10,14]; these values are much greater than the current values. This is attributed to Al^{3+} entering the lattice of crystalline SiO_2, creating additional oxygen vacancies. These results indicate that a discrete distribution of HfO_2 particles in Si–HfO_2 composites can form a continuous thin SiO_2 "mortar", achieving a comparable oxidation rate to that of pure Si while suppressing phase-transition-induced cracking.

To minimize the SiO_2 phase transition, a high concentration of HfO_2 was added to the Si–HfO_2 composite coatings [13,16,23,25]. However, both continuous HfO_2 and $HfSiO_4$ act as oxygen conduits [17,21], resulting in a greater oxidation rate. The current study demonstrated that a discrete distribution of HfO_2 particles in Si–HfO_2 composites can yield a comparable oxidation rate to that of pure Si (Fig. 6).

4.4 $HfSiO_4$ formation kinetics

In Si–HfO_2 composite coatings, the suppression of the SiO_2 phase transition is achieved through the reaction between SiO_2 and HfO_2 to form $HfSiO_4$ [13,16,17]. Therefore, achieving synergy between oxidation (formation of SiO_2) and reaction (formation of $HfSiO_4$) kinetics is crucial for minimizing the SiO_2 content. Figures 7 and 8 show the surface and cross-sectional microstructures of the $HfSiO_4$ particles after oxidation at 1370 ℃. Compared to those of the HfO_2 particles in the as-prepared composites (Figs. 2(a) and 2(b)), the sizes of the $HfSiO_4$ particles significantly increased (Fig. 7 and Table 2). However, the size of the HfO_2 particles inside the composites remained relatively unchanged with increasing duration (Fig. 5), indicating high thermal stability at 1370 ℃. The residual HfO_2 phases inside the $HfSiO_4$ particles exhibit a discrete island distribution. These findings suggest that a large $HfSiO_4$ island formed through the coalescence of smaller $HfSiO_4$ particles rather than through the coalescence of HfO_2 particles. The formation of $HfSiO_4$ occurs through the inward diffusion of SiO_2, consistent with the findings of a previous report indicating that the diffusion of Hf^{4+} is much slower than that of Si^{4+} and O^{2-} [34]. This difference is attributed to the much larger ionic radius of Hf^{4+} (0.83 Å) compared to that of Si^{4+} (0.54 Å) [32], coupled with the stronger interaction between Hf^{4+} and O^{2-}. Furthermore, the $HfSiO_4$ particles were enriched on the surface of the SiO_2 scale (Fig. 8), indicating phase separation between $HfSiO_4$ and SiO_2. This is consistent with the XRD results (Fig. 3(d)). As the oxidation time increases from 10 to 100 h at 1370 ℃, the average $HfSiO_4$ particle size increases from 1.10 to 1.28 μm in the Si20Hf composites (Table 2) and from 1.75 to 2.02 μm in the Si30Hf composites. A larger $HfSiO_4$ particle size is not conducive to improving the cracking resistance, as evidenced by cracks forming through the $HfSiO_4$ particles (Figs. 7(b) and 7(f)). Additionally, compared to that on the Si30Hf composite, the HfO_2 phase on the surface of the Si20Hf composite was almost completely consumed after 100 h of oxidation (Fig. 7(e)), effectively minimizing the SiO_2 content. These results indicate that the Si–HfO_2 composites with 20 mol% HfO_2 demonstrate optimal resistance to cracking and oxidation.

4.5 Cracking behavior

Due to phase-transition-induced cracking [10,13,14], networked cracks and interfacial delamination were observed on the surface of pure Si after 10 h of oxidation at 1300 ℃ (Fig. 9(a)). The SiO_2 thickness is ~1.7 μm after 10 h of oxidation at 1300 ℃ (Fig. 6), which is consistent with the reported occurrence of channel cracking when the SiO_2 TGO thickness exceeds ~1.5 μm [8,13]. Similarly, networked cracks were observed on the Si10Hf composite (Fig. 9(b)), where the TGO thickness was ~2.0 μm. This indicates that the addition of 10 mol% HfO_2 fails to suppress phase-transition-induced cracking. This is consistent with the prediction that the stress in the Si10Hf composite was reduced by only 9% compared to that in pure Si (Fig. 1(e)) and that the critical TGO thickness (h_c, Eq. (1)) in the Si10Hf composite was only ~1.6 μm (Fig. 1(f)). This was confirmed by the observation of network cracks in the Si–HfO_2 coating with 11.7 mol% HfO_2 after 10 h of oxidation at 1300 ℃ [35]. However, few discrete cracks were observed on the surface of the Si20Hf and Si30Hf composites after 100 h of oxidation at 1370 ℃ (Figs. 9(d) and 9(e)), although the TGO thicknesses reached 5.4 and 9.4 μm, respectively. However, widespread delamination occurs in pure Si when the TGO thickness reaches 5.0 μm [9,10,14]. These results indicate that, compared with the service lifetime of pure Si, the lifetimes of

Table 1 Fitted growth rate for Si–HfO_2 composites during isothermal oxidation according to the data in Fig. 6 (Unit: μm·$h^{-1/2}$)

Temperature (℃)	Si	Si10Hf	Si20Hf	Si30Hf
1300	0.46	0.48	0.54	0.83
1370	0.61	0.57	0.63	0.97

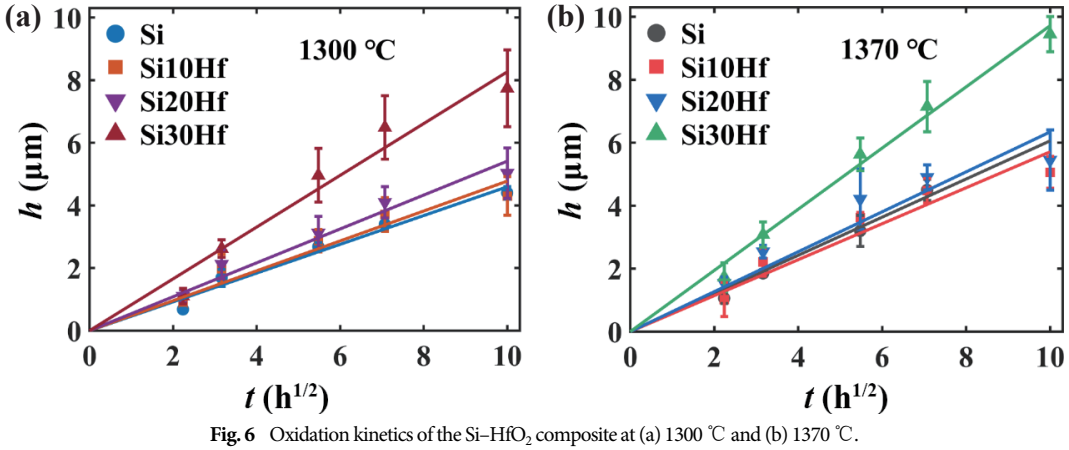

Fig. 6 Oxidation kinetics of the Si–HfO_2 composite at (a) 1300 ℃ and (b) 1370 ℃.

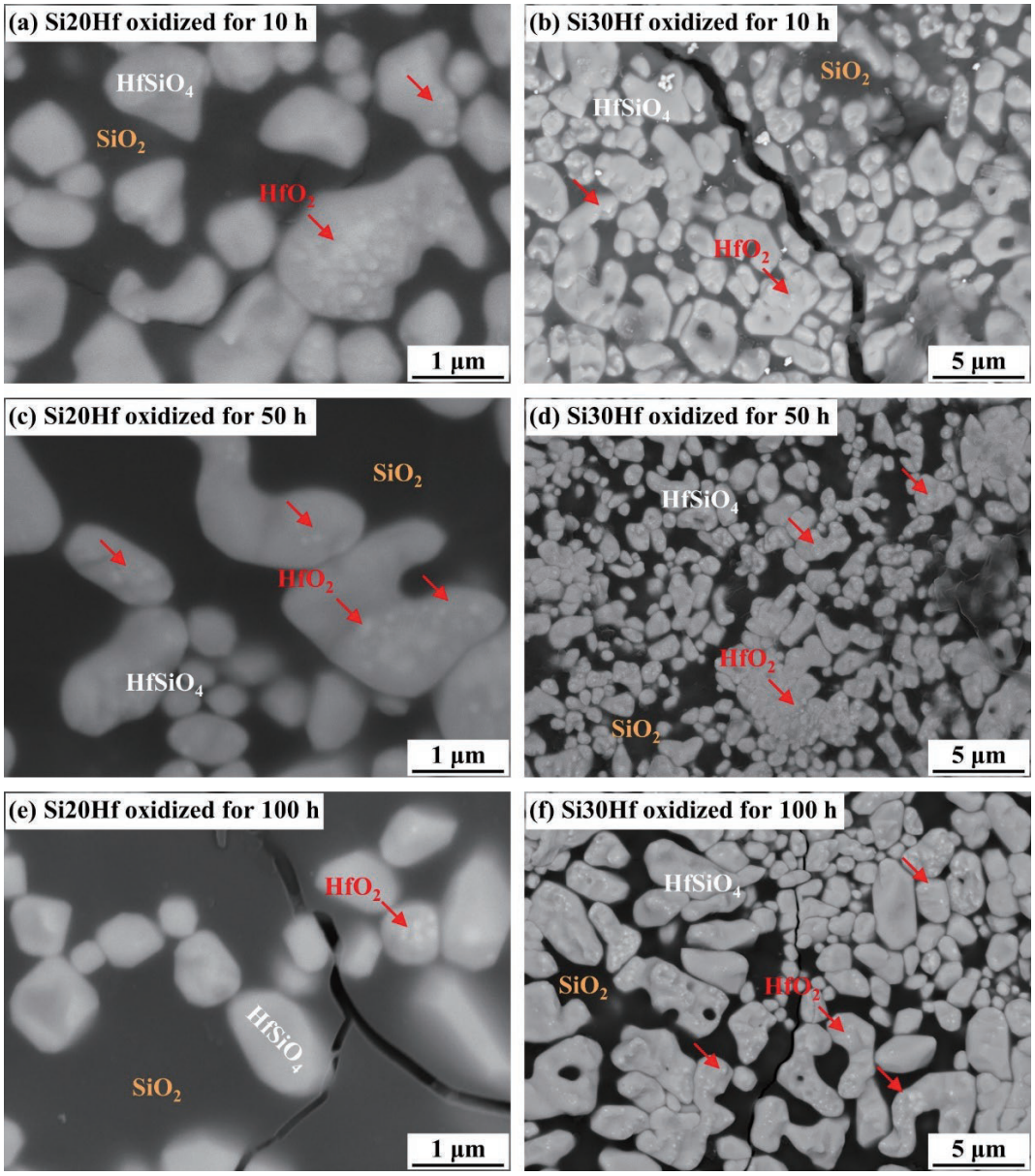

Fig. 7 Surface morphologies of (a, c, e) Si20Hf and (b, d, f) Si30Hf composites after isothermal oxidation for 10, 50, and 100 h at 1370 ℃.

the Si20Hf and Si30Hf composites at 1370 ℃ increase by more than 10 times.

The crack widths in the Si10Hf and Si20Hf composites are smaller than those in pure Si (Figs. 9(b) and 9(d)). The crack width (w) is proportional to the cracking strain [29], and it dictates

$$w = g_1 \varepsilon_0 h \tag{2}$$

where g_1 is a dimensionless parameter and h is the TGO thickness. For no elastic mismatch, g_1 = 5.816 [29]. Due to the discrete distribution of HfO_2 and $HfSiO_4$ particles (Figs. 4(b) and 4(d)), the Si10Hf and Si20Hf composites have TGO thicknesses comparable to that of pure Si (Fig. 6 and Table 1). This indicates that HfO_2 addition reduces the cracking stress induced by the SiO_2 phase transition. Furthermore, the crack path is along the edge of the $HfSiO_4$ particles (Figs. 9(b) and 9(d)), which is consistent with the fact that $HfSiO_4$ has a larger fracture toughness than SiO_2 [10,20]. However, although more $HfSiO_4$ is formed on the Si30Hf surface, the crack width is much larger than that in the pure Si and Si20Hf composites (Fig. 9(d)). This is because the TGO thickness of the Si30Hf composites is much greater than that of pure Si (Fig. 6 and Table 1). These results indicate that the cracking in Si–HfO_2 composites relies on both the content of $HfSiO_4$ particles and the thickness of the SiO_2 scale.

The crack spacing (S) is inversely proportional to the cracking strain [29] and dictates

$$S = 2g_2 h \cdot \operatorname{arctanh}\left(\frac{\gamma}{g_2 h \bar{E} \varepsilon_0^2}\right) \tag{3}$$

where g_2 is a dimensionless parameter and the symbol arctanh represents the inverse hyperbolic tangent function. For no elastic mismatch, g_2 = 1.976 [29]. The crack spacing of the Si10Hf composite is comparable to that of pure Si (Figs. 9(a) and 9(b)). However, the crack spacing in the Si20Hf composites is much greater than that in the pure Si and Si10Hf composites (Figs. 9(a), 9(b), and 9(d)). The Si20Hf composite has a TGO thickness comparable to that of the pure Si and Si10Hf composites (Fig. 6). This indicates that the cracking strain (ε_0) in the Si20Hf composite

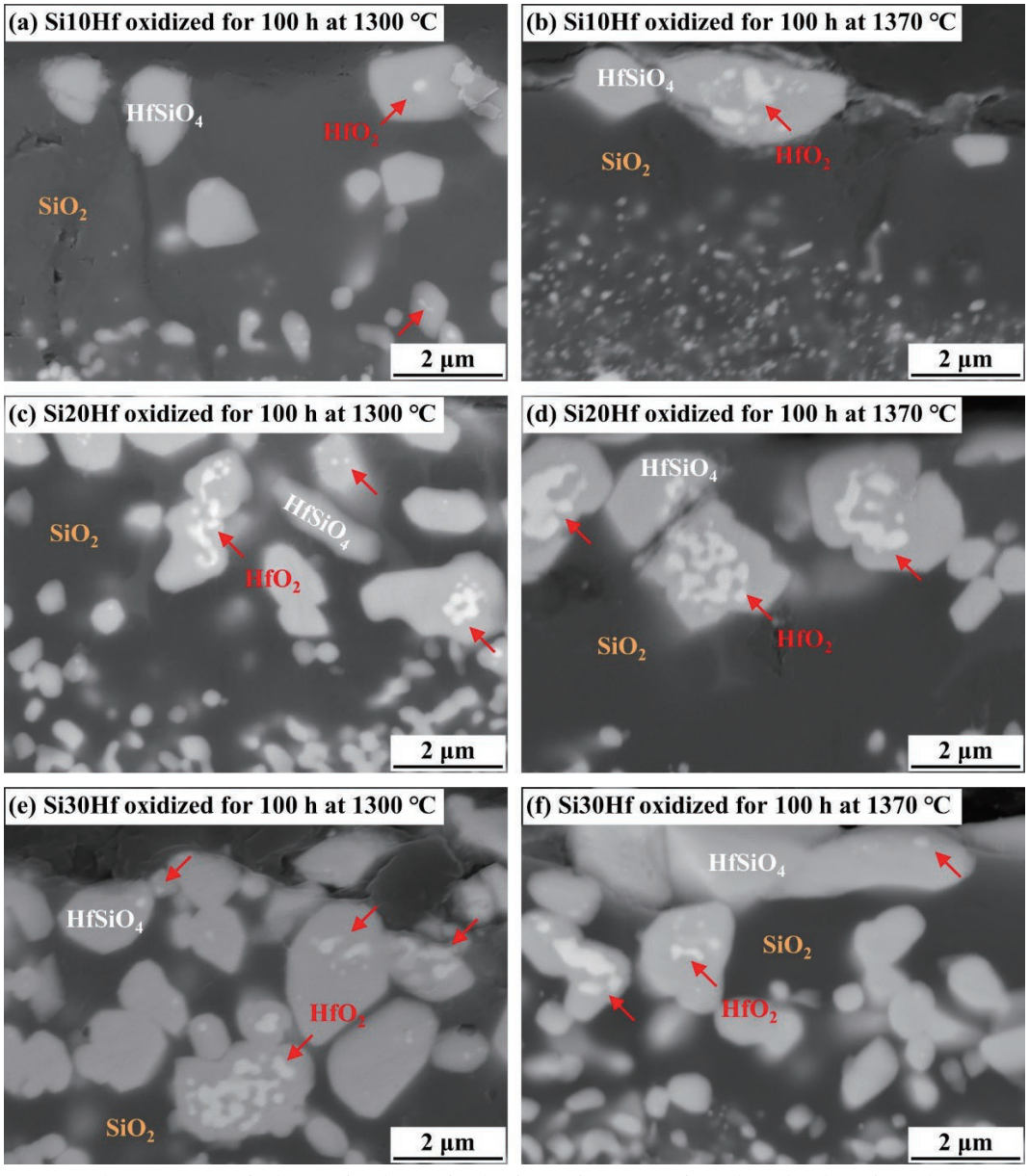

Fig. 8 Cross-sectional microstructures of (a, b) Si10Hf, (c, d) Si20Hf, and (e, f) Si30Hf composites after isothermal oxidation for 100 h at 1300 and 1370 ℃.

Table 2 Average $HfSiO_4$ particle size during oxidation at 1370 ℃ (Unit: μm)

Duration (h)	Si10Hf	Si20Hf	Si30Hf
1	0.72	0.81	0.93
10	1.09	1.10	1.75
100	1.18	1.28	2.02

is much lower than that in the pure Si and Si10Hf composites. This is consistent with the smaller cracking strain (ε_0) in the Si20Hf composite due to the higher $HfSiO_4$ content.

In brief, premature channel cracking occurred in the Si10Hf composite, indicating that the addition of 10 mol% HfO_2 failed to suppress phase transition-induced cracking. Although it has a larger crack spacing than that in the pure Si and Si10Hf composites, the Si30Hf composite has a larger crack width, indicating a smaller cracking strain and a larger TGO thickness. Among all the composites, Si20Hf has the smallest crack width and the largest spacing, indicating the optimal resistance to cracking and oxidation.

5 Discussion

5.1 Phase separation between $HfSiO_4$ and SiO_2

To elucidate the reason for phase separation, the surface and interface energies of $HfSiO_4$–SiO_2 and HfO_2–SiO_2 were investigated through first-principles calculations. The results reveal that $HfSiO_4$ has a significantly lower surface energy than the interface energy between $HfSiO_4$ and SiO_2 (Fig. 10(a)). Additionally, the presence of vacancies at the interface between $HfSiO_4$ and SiO_2 also indicates susceptibility to phase separation (Fig. 10(c)). Moreover, the low overlap of the density of state peaks between SiO_2 and $HfSiO_4$ (only three peaks) suggests

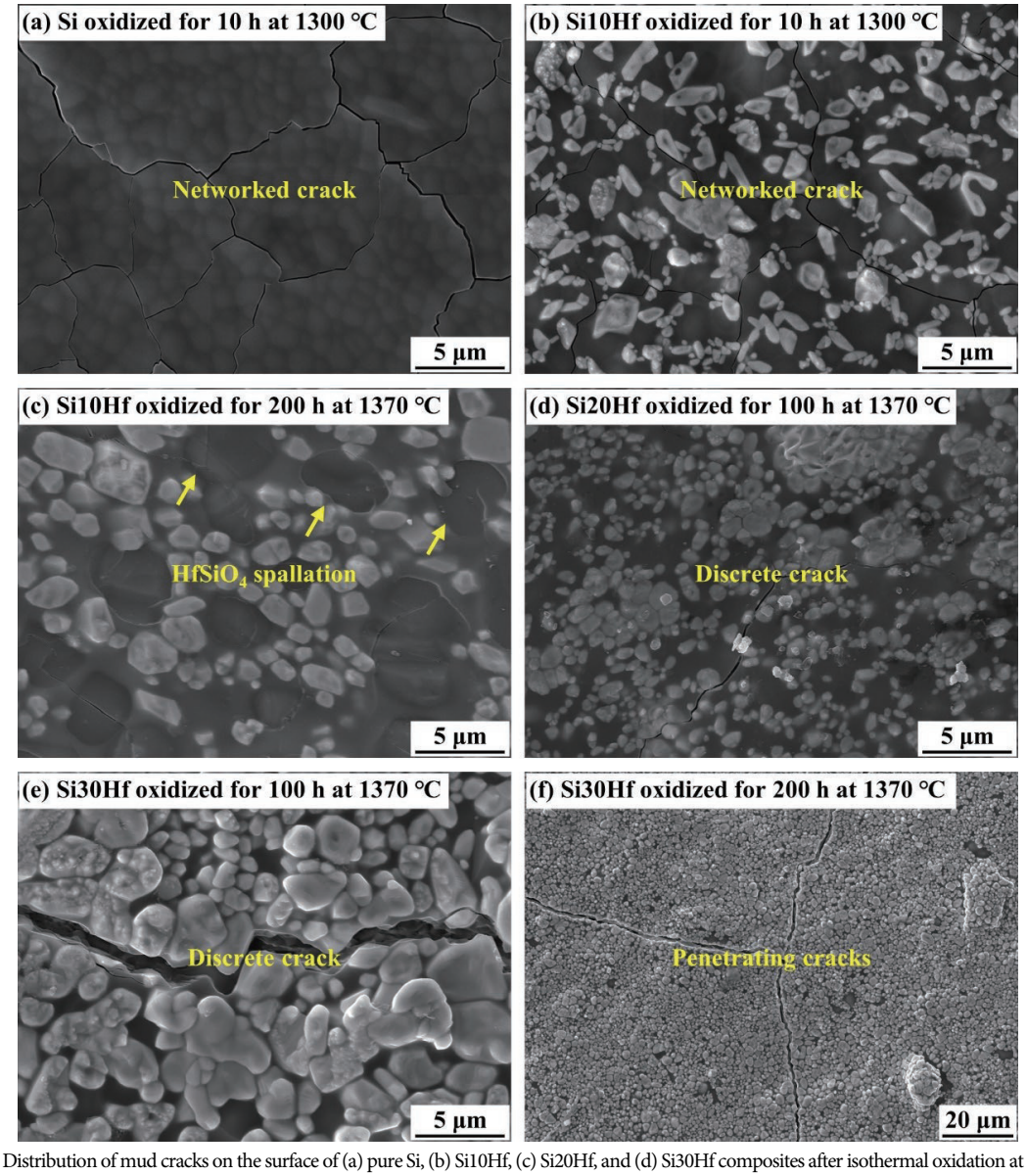

Fig. 9 Distribution of mud cracks on the surface of (a) pure Si, (b) Si10Hf, (c) Si20Hf, and (d) Si30Hf composites after isothermal oxidation at 1370 ℃.

susceptibility to phase separation (Fig. 10(d)). The total band gaps at the $HfSiO_4$–SiO_2 and HfO_2–SiO_2 interfaces are much narrower than those at the pure SiO_2, $HfSiO_4$, and HfO_2 phases, and they exhibit a leftward shift (Fig. 10(d)). This difference implies the possible presence of electron holes at the interface, indicating the instability of the $HfSiO_4$–SiO_2 and HfO_2–SiO_2 interfaces. HfO_2 also has a lower surface energy than the interface energy between HfO_2 and SiO_2 (Fig. 10(b)), signifying a substantial reaction driving force between HfO_2 and SiO_2. This was confirmed by the formation of the tetragonal $HfSiO_4$ phase after only 5 h of isothermal oxidation (Fig. 3). These results indicate that the future direction for better antioxidative Si–HfO_2 composite coatings is to inhibit the phase separation between $HfSiO_4$ and SiO_2 while retaining the discrete distribution of the HfO_2 phase.

5.2 Ion migration mechanism

Figure 11 shows the TEM images of the Si30Hf composite after oxidation at 1370 ℃. The $HfSiO_4$ phase exhibited a continuous distribution inside the scale (Figs. 11(a) and 11(d)). By acting as an oxygen conduit, the continuous $HfSiO_4$ phase contributed to a greater oxidation rate than that of pure Si and Si20Hf (Fig. 6 and Table 1). Moreover, due to phase separation, $HfSiO_4$ phases were enriched at the surface (Figs. 11(a) and 11(d)). Phase separation results in the formation of a SiO_2-rich zone underneath the $HfSiO_4$ layer (Fig. 11(a)). Due to the SiO_2-rich zone, the oxidation rate is lower than that of Si-stabilizer duplex coatings [14]. In line with the XRD results (Fig. 3), tetragonal $HfSiO_4$ and α-SiO_2 were detected (Figs. 11(b) and 11(c)). Additionally, a large $HfSiO_4$ island is formed by the agglomeration of smaller particles (Fig. 11(a)). This suggests that the formation of $HfSiO_4$ occurs through the inward diffusion of SiO_2. This is consistent with the smaller crystalline plane spacing of SiO_2 compared to that of $HfSiO_4$ and HfO_2 (Figs. 11(e) and 11(f)).

5.3 Implications for more durable EBCs

Compared to those of a pure Si coating, the Si–HfO_2 bond coating exhibits a significantly greater strength (~90 MPa) and creep rate (~10^{-6} s^{-1}) at 1400 ℃ [36]. However, reports indicate that the free Si within a 50 μm thick Si–HfO_2 coating (25/75 mol% HfO_2/Si) was completely oxidized within 10 h at 1371 ℃ [17]. This rapid oxidation is attributed to the continuous distribution of the HfO_2 phase, which serves as an oxygen conduit. Conversely, the

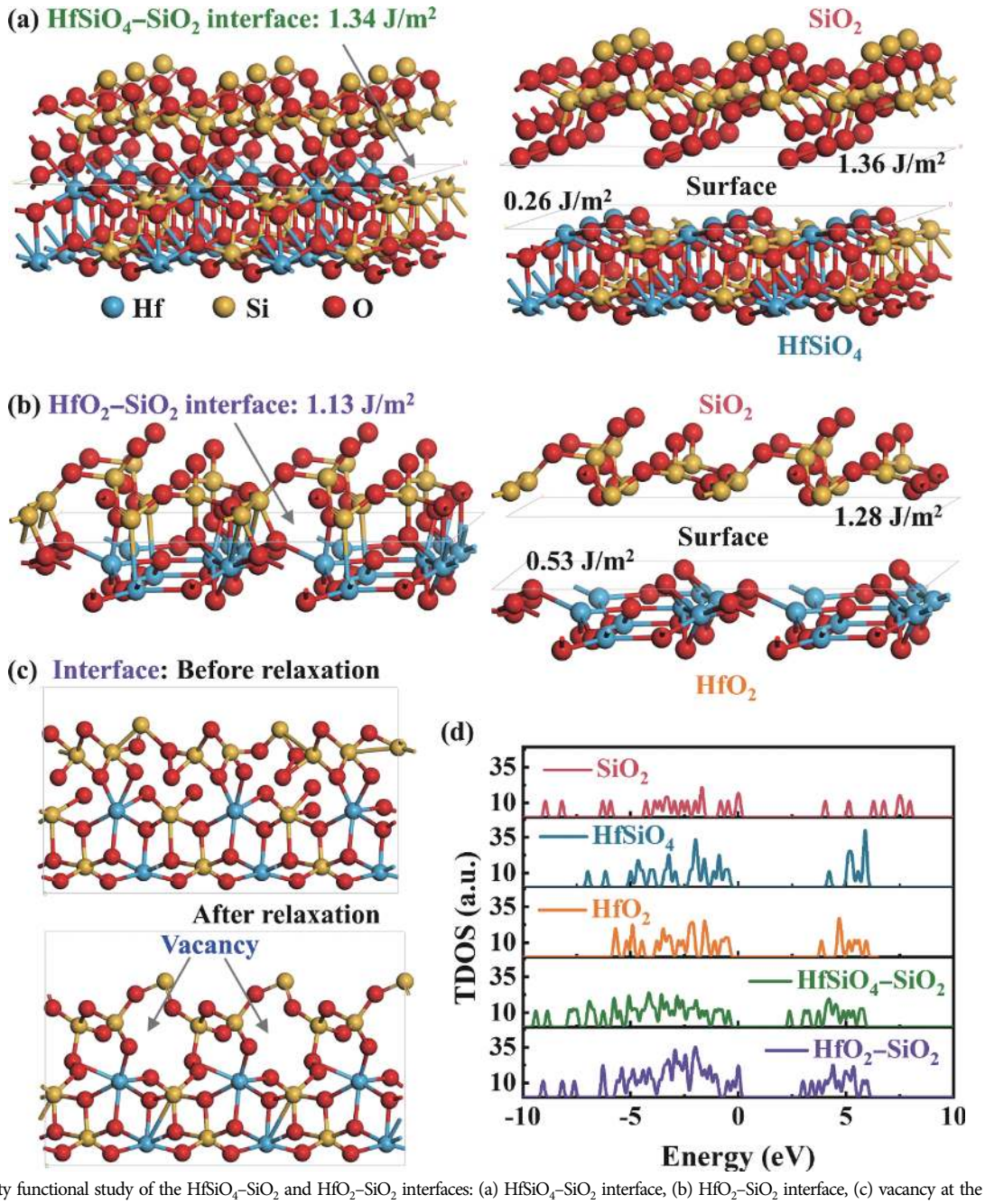

Fig. 10 Density functional study of the $HfSiO_4$–SiO_2 and HfO_2–SiO_2 interfaces: (a) $HfSiO_4$–SiO_2 interface, (b) HfO_2–SiO_2 interface, (c) vacancy at the $HfSiO_4$–SiO_2 interface, and (d) total density of states.

composites with 10 and 20 mol% HfO_2 exhibit oxidation rates comparable to those of pure Si (Fig. 6 and Table 1). These findings emphasize the importance of maintaining a discrete distribution of the HfO_2 phase for enhanced oxidation resistance. Moreover, the coefficients of thermal expansion (CTEs) of the pure HfO_2 and Si–HfO_2 composites are 5.8×10^{-6} K^{-1} and 5×10^{-6}–6×10^{-6} K^{-1} [15–17,22], respectively, both of which are greater than those of SiC_f/SiC CMCs [10]. This suggests potential tensile stresses in the composite during thermal cycling, leading to vertical cracking and interfacial delamination [18]. Therefore, controlling the HfO_2 content while maintaining a discrete distribution is crucial.

The suppression of the SiO_2 phase transition within the Si–HfO_2 composite relies on the reaction between SiO_2 and HfO_2. If the HfO_2 content falls below a critical level, phase-transition-induced cracking is likely to occur, as evidenced by the mud cracking in the Si10Hf composite (Fig. 9(b)). Additionally, the continuous distribution of HfO_2 in the Si30Hf composites results in an oxidation rate 1.8 times greater than that of pure Si at 1370 ℃ (Fig. 6 and Table 1). These results highlight that the composite with 20 mol% HfO_2 exhibits optimal resistance to cracking and oxidation. This insight is crucial for designing Si–HfO_2 powders and coatings to achieve extended service lifetimes at 1370 ℃.

The CTE of $HfSiO_4$ is approximately 3.65×10^{-6}–4.55×10^{-6} K^{-1} [15,16,18,37], which matches that of SiC and Si [10]. However, due to the significantly lower surface energy of $HfSiO_4$ (Fig. 10), phase separation occurred between $HfSiO_4$ and SiO_2 during oxidation (Figs. 4 and 8). This phase separation is not conducive to inhibiting phase-transition-induced cracking and may lead to the formation of a fluorite-structured HfO_2 phase (F_{SS}-HfO_2) at the HfO_2/$Yb_2Si_2O_7$ interface [22,38]. The CTE of F_{SS}-HfO_2 is much larger than that of the m-HfO_2 and SiC substrates, causing premature spallation of the EBCs. Thus, a promising avenue for

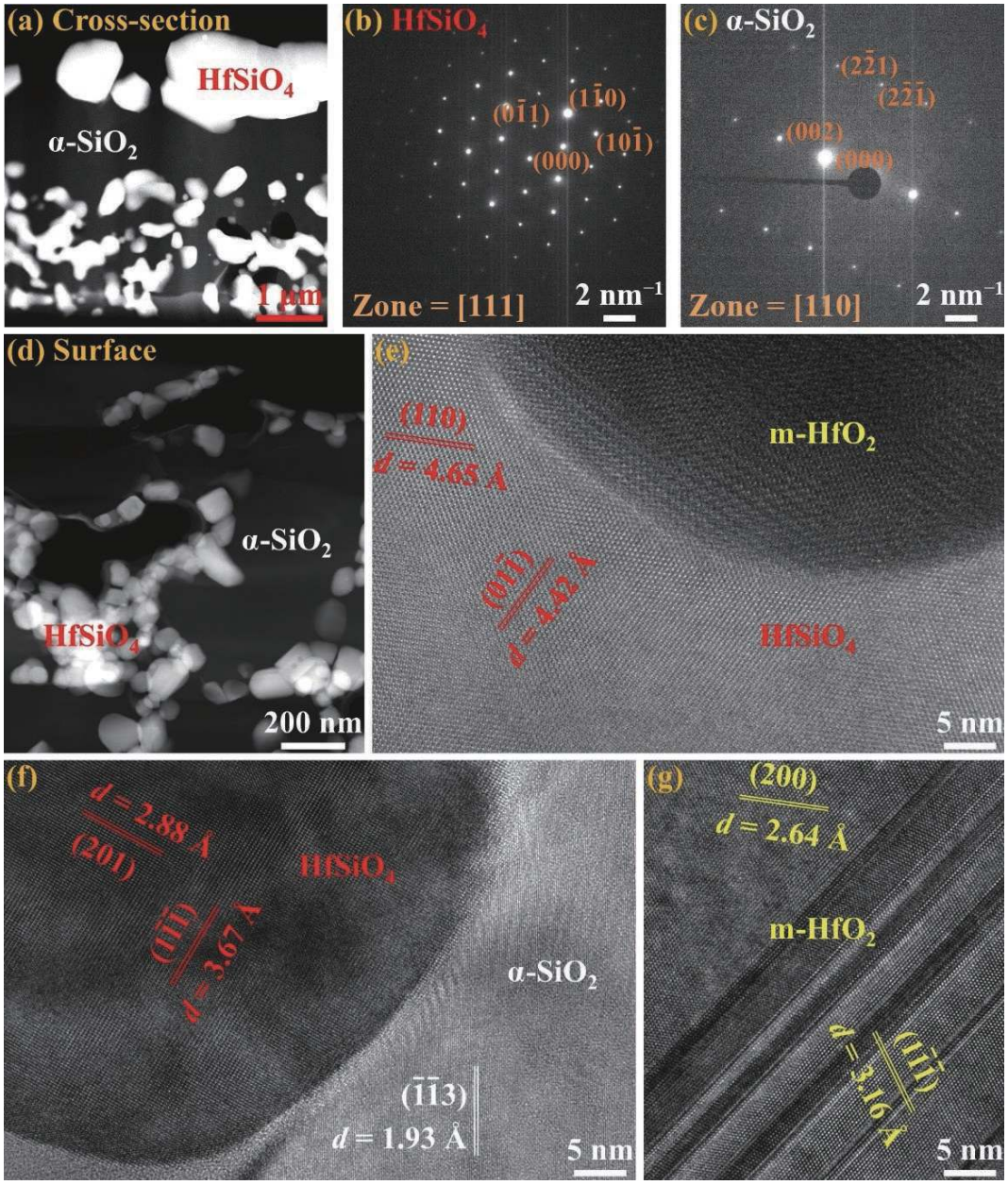

Fig. 11 TEM characterization results of Si–HfO_2 composite samples after isothermal oxidation at 1370 ℃: (a, d) cross-section and surface images, (b, c) selected-area diffraction (SAD) patterns of $HfSiO_4$ and α-SiO_2, (e, f) HRTEM images at the HfO_2/$HfSiO_4$ and $HfSiO_4$/SiO_2 interfaces, and (g) HRTEM image of m-HfO_2.

improving antioxidative Si–HfO_2 composite coatings involves inhibiting phase separation between $HfSiO_4$ and SiO_2 while retaining the discrete distribution of the HfO_2 phase.

6 Conclusions

In this study, Si–HfO_2 dual-state duplex composite materials are proposed to enhance both the oxidation resistance and cracking resistance. The structural evolution, oxidation kinetics, and cracking behavior of the composite were characterized. The main conclusions are as follows:

1) The as-prepared composite has a structure comprising discrete HfO_2 "bricks" embedded in a continuous Si "mortar", while the oxidized state transforms into discrete $HfSiO_4$ "bricks" within continuous thin SiO_2 "mortars".

2) The continuous thin SiO_2 "mortars" effectively inhibit oxygen permeation, enabling the composite with 20 mol% HfO_2 to achieve an oxidation rate comparable to that of pure Si at 1300 and 1370 ℃, despite the oxygen-conducting role of $HfSiO_4$.

3) Discrete $HfSiO_4$ particles are beneficial for relieving phase-transition-induced stress and hindering crack propagation. Consequently, the lifetime of the composite with 20 mol% HfO_2 exceeds that of pure Si by more than 10 times at 1370 ℃.

Acknowledgements

This study is supported by the Postdoctoral Innovative Talent Support Program (No. BX2021238), the National Natural Science Foundation of China (No. U22A20110), and the Natural Science Foundation of Suzhou (No. SYG202103).

Declaration of competing interest

The authors have no competing interests to declare that are relevant to the content of this article. The author Guanjun Yang is the Editorial Committee member of this journal.

References

[1] Padture NP. Advanced structural ceramics in aerospace propulsion. *Nat Mater* 2016, **15**: 804–809.

[2] Chen PJ, Xiao P, Tang X, *et al*. Corrosion behavior and failure mechanism of SiC whisker and c-$AlPO_4$ particle-modified novel tri-layer $Yb_2Si_2O_7$/mullite/SiC coating in burner rig tests. *J Adv Ceram* 2022, **11**: 1901–1917.

[3] Padture NP. Environmental degradation of high-temperature protective coatings for ceramic-matrix composites in gas-turbine engines. *NPJ Mater Degrad* 2019, **3**: 11.

[4] Leisner V, Kelm K, Schulz U. Thin single-phase yttrium-based environmental barrier coating systems for SiC/SiC CMCs. *J Eur Ceram Soc* 2022, **42**: 7275–7287.

[5] Dong L, Liu MJ, Zhang XF, *et al*. Pressure infiltration of molten aluminum for densification of environmental barrier coatings. *J Adv Ceram* 2022, **11**: 145–157.

[6] Xiang HM, Xing Y, Dai FZ, *et al*. High-entropy ceramics: Present status, challenges, and a look forward. *J Adv Ceram* 2021, **10**: 385–441.

[7] Chen ZL, Tian ZL, Zheng LY, *et al*. $(Ho_{0.25}Lu_{0.25}Yb_{0.25}Eu_{0.25})_2SiO_5$ high-entropy ceramic with low thermal conductivity, tunable thermal expansion coefficient, and excellent resistance to CMAS corrosion. *J Adv Ceram* 2022, **11**: 1279–1293.

[8] Richards BT, Young KA, de Francqueville F, *et al*. Response of ytterbium disilicate–silicon environmental barrier coatings to thermal cycling in water vapor. *Acta Mater* 2016, **106**: 1–14.

[9] Bakan E, Vaßen R. Oxidation kinetics of atmospheric plasma sprayed environmental barrier coatings. *J Eur Ceram Soc* 2022, **42**: 5122–5128.

[10] Chen L, Li JH, Wang GQ, *et al*. Improving oxidation resistance of Si coating by isolated-particle healing. *Corros Commun* 2022, **8**: 9–17.

[11] Richards BT, Sehr S, de Franqueville F, *et al*. Fracture mechanisms of ytterbium monosilicate environmental barrier coatings during cyclic thermal exposure. *Acta Mater* 2016, **103**: 448–460.

[12] Chen DY, Harmon R, Dwivedi G, *et al*. In-flight particle states and coating properties of air plasma sprayed ytterbium disilicates. *Surf Coat Technol* 2021, **417**: 127186.

[13] Anton R, Leisner V, Watermeyer P, *et al*. Hafnia-doped silicon bond Coats manufactured by PVD for SiC/SiC CMCs. *Acta Mater* 2020, **183**: 471–483.

[14] Chen L, Wang WJ, Li JH, *et al*. Suppressing the phase-transition-induced cracking of SiO_2 TGOs by lattice solid solution. *J Eur Ceram Soc* 2023, **43**: 3201–3215.

[15] Bakan E, Sohn YJ, Vaßen R. Microstructure and phase composition evolution of silicon-hafnia feedstock during plasma spraying and following cyclic oxidation. *Acta Mater* 2021, **214**: 117007.

[16] Li G, Lu XR, Huang JQ, *et al*. Thermal cycling behavior and failure mechanism of the Si–HfO_2 environmental barrier coating bond coats prepared by atmospheric plasma spraying. *J Alloys Compd* 2022, **913**: 165319.

[17] Harder BJ. Oxidation performance of Si–HfO_2 environmental barrier coating bond coats deposited via plasma spray-physical vapor deposition. *Surf Coat Technol* 2020, **384**: 125311.

[18] Li G, Li JY, Chen WB, *et al*. Cyclic oxidation and water vapor corrosion behaviors of multi-layer environmental barrier coatings with HfO_2–Si bond coat for SiCf/SiC. *Mater Chem Phys* 2022, **292**: 126768.

[19] Liu RX, Liang WP, Miao Q, *et al*. Micromechanical analysis and theoretical predictions towards thermal shock resistance of HfO_2–Si environmental barrier coatings. *Compos Part B Eng* 2021, **226**: 109334.

[20] Robertson AL, Solá F, Zhu DM, *et al*. Microscale fracture mechanisms of HfO_2–Si environmental barrier coatings. *J Eur Ceram Soc* 2019, **39**: 2409–2418.

[21] Shinoda Y, Marshall DB, Raj R. Oxidation, mechanical and thermal properties of hafnia–silicon carbide nanocomposites. *J Eur Ceram Soc* 2014, **34**: 1783–1790.

[22] Deijkers JA, Wadley HNG. A duplex bond coat approach to environmental barrier coating systems. *Acta Mater* 2021, **217**: 117167.

[23] Ding QJ, Tan X, Jiang LW, *et al*. High-temperature performances of Si–HfO_2-based environmental barrier coatings via atmospheric plasma spraying. *Ceram Int* 2022, **48**: 23127–23136.

[24] Parmigiani J, Thouless M. The roles of toughness and cohesive strength on crack deflection at interfaces. *J Mech Phys Solids* 2006, **54**: 266–287.

[25] Chen WB, Han QZ, He J, *et al*. Effect of HfO_2 framework on steam oxidation behavior of HfO_2 doped Si coating at high temperatures. *Ceram Int* 2022, **48**: 20201–20210.

[26] Chen DY. Suspension HVOF sprayed ytterbium disilicate environmental barrier coatings. *J Therm Spray Technol* 2022, **31**: 429–435.

[27] Chen L, Yang B, Li GR, *et al*. Thermochemical stability of $Yb_2Si_2O_7$ environmental barrier coatings during thermal cycling and water vapor corrosion at 1350 ℃. *J Therm Spray Technol* 2023, **32**: 1811–1827.

[28] Anton R, Leisner V, Schulz U. Nanoindentation dataset of silicon and hafnia doped silicon coatings produced by magnetron sputtering. *Data Brief* 2020, **31**: 105800.

[29] Hutchinson JW, Suo Z. Mixed mode cracking in layered materials. In: *Advances in Applied Mechanics*. Amsterdam: Elsevier, 1991: 63–191.

[30] Deijkers JA, Wadley HNG. Hafnium silicate formation during oxidation of a permeable silicon + HfO_2 powder composite system. *Acta Mater* 2020, **201**: 448–461.

[31] Chen DY. TGO growth behavior in environmental barrier coatings with modified silicon bond coat. *J Therm Spray Technol* 2023, https://doi.org/10.1007/s11666-023-01688-x

[32] Johnson B, Jones JL. Structures, phase equilibria, and properties of HfO_2. In: *Ferroelectricity in Doped Hafnium Oxide: Materials, Properties and Devices*. Amsterdam: Elsevier, 2019: 25–45.

[33] Chen L, Meng GH, Li CJ, *et al*. Critical scale grain size for optimal lifetime of TBCs. *J Mater Sci Technol* 2022, **115**: 241–250.

[34] Cherniak DJ. Si diffusion in zircon. *Phys Chem Miner* 2008, **35**: 179–187.

[35] Xiao SK, Li JZ, Liu XR, *et al*. Exploration of the oxidation behavior and doping ratio of the Si–HfO_2 bond layer used in environmental barrier coatings. *Int J Appl Ceram Technol* 2023, **20**: 1753–1763.

[36] Zhu D. Development and performance evaluations of HfO_2–Si and rare earth-Si based environmental barrier bond coat systems for SiC/SiC ceramic matrix composites. https://ntrs.nasa.gov/api/citations/20140008956/downloads/20140008956.pdf

[37] Ding ZD, Ridley M, Deijkers J, *et al*. The thermal and mechanical properties of hafnium orthosilicate: Experiments and first-principles calculations. *Materialia* 2020, **12**: 100793.

[38] Deijkers JA, Begley MR, Wadley HNG. Failure mechanisms in model thermal and environmental barrier coating systems. *J Eur Ceram Soc* 2022, **42**: 5129–5144.